



1 **Lahar events in the last 2,000 years from Vesuvius eruptions. Part**
2 **2: Formulation and validation of a computational model based on**
3 **a shallow layer approach**

4 Mattia de' Michieli Vitturi¹, Antonio Costa², Mauro A. Di Vito³, Laura Sandri², Domenico M.
5 Doronzo³

6

7 ¹Istituto Nazionale di Geofisica e Vulcanologia, Sezione di Pisa, Pisa, 56125, Italy

8 ²Istituto Nazionale di Geofisica e Vulcanologia, Sezione di Bologna, Bologna, 40128, Italy

9 ³Istituto Nazionale di Geofisica e Vulcanologia, Osservatorio Vesuviano, Napoli, 80124, Italy

10 *Correspondence to:* Mattia de' Michieli Vitturi (mattia.demichielivitturi@ingv.it)

11 **Abstract.** In this paper we present a new model for the simulation of lahars, based on the depth-averaged code IMEX-
12 SfloW2D with new governing and constitutive equations introduced to better describe the dynamics of lahars. A thorough
13 sensitivity analysis is carried out to identify the critical processes (such as erosion and deposition) and parameters (both
14 numerical and physical) controlling lahar runout, using both synthetic and real cases topographies. In particular, an
15 application of the model to a syn-eruptive lahar from a reference-size eruption from Somma-Vesuvius, affecting the
16 Campanian Plain (Southern Italy), described in Di Vito et al. (this issue), is used in this work for the sensitivity analysis.
17 Effects of erosion and deposition are investigated by comparing simulations with and without these processes. By
18 comparing flow thickness and area covered by the flow and their evolution with time, we show that the modelling of both
19 the processes is important to properly simulate the effects of the bulking and debulking and the associated changes in
20 rheology. From a computational point of view, the comparison of simulations obtained for different numerical grids (from
21 25 m to 100 m), scheme order, and grain size discretization were useful to find a good compromise between resolution
22 and computational speed. The companion paper by Sandri et al. (this issue) shows an application of the presented model
23 for probabilistic volcanic hazard assessment for lahars from Vesuvius deposits in the Neapolitan area.

24 **1 Introduction**

25 Water saturated flows made from volcanic deposits are known as “lahar”, an Indonesian term used to indicate muddy
26 flows. As typical in the volcanological literature, here we will use the term lahar to denote any water saturated flows,
27 from hyperconcentrated flow, carrying up to 50 vol % sediment, to lower concentration flows (< 10 % sediment). These
28 wet granular flows are commonly characterised by a high flow density and can have high flow velocity, generating large
29 dynamic pressures able to destroy even buildings and infrastructures. Moreover, this kind of flows can inundate large
30 areas, disrupting ground transportation networks, human settlements, power lines, industry, agriculture (e.g., Zanchetta
31 et al., 2004).

32 Lahars can form from the remobilization of unconsolidated tephra, as for the hundreds of lahars generated by torrential
33 rains after the 1991 Pinatubo eruptions in the Philippines (Van Westen and Daag, 2005). In other cases, as at Mount St.
34 Helens, lahars can result from dome collapses and the associated volcanic explosions (Scott, 1988). Additionally,



35 devastating lahars can form when a pyroclastic flow melts snow or ice caps (Major and Newhall, 1989), as occurred for
36 the 1995 eruption on the glaciated Nevado del Ruiz, Colombia (Pierson et al., 1990). Mt. Rainier is another example of
37 volcano that experienced several lahars of this kind in the past. Lahars can form also in eruptions beneath crater lakes, as
38 at Keluth, Indonesia (Mastin and Witter, 2000) and Ruapehu, New Zealand (Lecointre et al., 2004).

39 If lahars are generated before, during, or after the eruption they are named pre-eruptive, syn-eruptive, or post-eruptive
40 lahars (Vallance and Iverson, 1995). The term syn-eruptive must not be taken literally, but indicates a lahar generated
41 during or in the period immediately following an eruption. Besides a triggering mechanism, generation of a lahar requires
42 *i)* an adequate water source, which can be hydrothermal water, rapidly melted snow and ice, crater lake water, and rainfall
43 runoff, *ii)* abundant unconsolidated debris that typically includes pyroclastic flow and fall deposits, glacial drift,
44 colluvium, and soil, and *iii)* steep slopes and substantial relief at the source (IAEA, 2016). Because lahars are water
45 saturated flows, for which both liquid and solid interactions are fundamental, their behaviour is different from other
46 related phenomena common to volcanoes such as debris avalanches and floods. In terms of fragment size distribution, the
47 material carried by lahars ranges in diameter from about 10^{-6} m to 10 m. Lahars can have temperature up to 100 °C and
48 can change character downstream, through processes of flow bulking (erosion and incorporation of secondary debris as
49 they move downstream) and debulking (a process in which the lahar selectively deposits certain particles, owing to their
50 size or density, as it moves downstream). Primary particles in lahar deposits derive from contemporaneous eruption
51 deposits or, in the case of avalanche induced lahar deposits, from the original avalanche mass; secondary particles derive
52 from the erosion and incorporation of downstream volcanoclastic debris, alluvium, colluvium glacial drift, bedrock, etc.
53 Many properties of lahars including, but not limited to, particle concentration, granulometry and componentry, bulk
54 rheology and velocity are highly variable in both time (i.e. unsteadiness) and space (i.e. non-uniformity).

55 Several methods have been proposed to assess the related hazard, ranging from simple empirical models like LAHARZ
56 (Iverson et al., 1998), which can be used to estimate the inundated areas, to geophysical mass-flow models which use
57 different rheological laws, such as Newtonian, Bingham, Bagnold, or Coulomb models, depending on flow behaviour,
58 (e.g., TITAN2D, Pitman et al., 2003; Patra et al., 2005; FLO2D, O'Brien et al., 1993; VolcFlow, Kelfoun and Druitt,
59 2005; Kelfoun et al., 2009) and can furnish values of critical variables, such as velocity and dynamic pressure. A different
60 approach, based on a fully three-dimensional model of two-phase flows, can be found in Dartevelle (2004) and Meruane
61 et al. (2010). One of the most general two-phase debris-flow models was developed by Pudasaini (2012), and it includes
62 many essential physical phenomena observable in debris flows. Mohr-Coulomb plasticity is used to close the solid stress.
63 The reader is addressed to Pudasaini (2012) and references therein for a general review of the topic. More recently,
64 building on the Pudasaini (2012) two-phase flow model, Pudasaini and Margili (2019) presented a new mass flow model
65 (r.avaflow, <https://www.landslidemodels.org/r.avaflow>) accounting for the complexity of geomorphic mass flows
66 consisting of coarse particles, fine particles, and viscous fluid.

67 In this work we present a new simplified model developed for the aim of lahar hazard assessment. The model, discussed
68 in Section 2, is based on the Saint-Venant depth-averaged equations, coupled with source terms accounting for friction
69 and with terms for erosion/deposition of solid particles. Then in Section 3 we present a few examples of model validation
70 and applications, and in Section 4 a short discussion and conclusion.

71 2 Physical-numerical model



72 The physical model for lahars is based on the shallow layer approach and on the solutions of a set of depth-averaged
73 transport equations. As we explain below numerical solution was obtained by modifying the IMEX-SfloW2D code (de'
74 Michieli-Vitturi et al., 2019), with new governing and constitutive equations introduced to better simulate lahars
75 dynamics. In this section, we briefly introduce all model variables, and we describe the governing equations.

76 2.1 Model governing equations

77 2.1.1 Depth-averaged transport equations

78 In this section, we present the set of partial differential equations governing the dynamics of lahars. Assuming that the
79 lahar flow is a homogeneous mixture of water and n_s solid phases (see Fig. 1), its density $\rho_m(x, y, t)$ is defined in terms
80 of the volumetric fractions $\alpha_{(c)}$ and densities $\rho_{(c)}$ of the components:

$$\rho_m = \alpha_w \rho_w + \sum_{i_s=1}^{n_s} \alpha_{s,i_s} \rho_{s,i_s} \quad (1)$$

81 where the subscript w denotes the water phase and the subscript s, i_s denote the class i_s of the solid phase. Equations are
82 written in global Cartesian coordinates (x, y) , with x and y orthogonal to the z -axis, assumed to be parallel to
83 gravitational acceleration $g = (0, 0, g)$. We denote the flow thickness with $h(x, y, t)$ and the depth-averaged horizontal
84 components of the flow velocity with $u(x, y, t)$ and $v(x, y, t)$, assuming that, due to the flow turbulence, solid phases are
85 well mixed with the liquid carrier phases, and they have the same horizontal velocity. The flow moves over a topography,
86 described by the variable $B(x, y, t)$. In principle, topography can change with time, but as first approximation we neglect
87 the changes associated with erosion and deposition, while these processes are modelled and accounted for the flow
88 dynamics. Thus, we assume the topography being a function of space only.

89 With the notation introduced above, conservation of mass for the flow mixture writes in the following way:

$$\frac{\partial \rho_m h}{\partial t} + \frac{\partial (\rho_m h u)}{\partial x} + \frac{\partial (\rho_m h v)}{\partial y} = \sum_{i_s=1}^{n_s} [\rho_{s,i_s} (E_{s,i_s} - D_{s,i_s})] + \rho_w \left\{ D_w + \frac{\alpha_d}{1 - \alpha_d} \sum_{i_s=1}^{n_s} [(E_{s,i_s} - D_{s,i_s})] \right\}, \quad (2)$$

90 where E_s and D_s are the volumetric rate of erosion and deposition of solid particles, respectively, and D_w is the rate of
91 loss of water, not associated with the deposition of particles (for example associated with evaporation or other processes).
92 The first term on the right-hand side accounts for the loss and entrainment of solid particles, while the last term accounts
93 for the loss of water. This term accounts not only for the loss due to the rate D_w , but also for the loss associated with
94 particle erosion and sedimentation. In fact, we assume both the pre-existing erodible layer and the flow deposit water-
95 saturated, with the volume fraction of water given by α_w .

96 The two equations for momentum conservation are:



$$\frac{\partial(\rho_m hu)}{\partial t} + \frac{\partial}{\partial x} \left(\rho_m hu^2 + \frac{1}{2} \rho_m gh^2 \right) + \frac{\partial}{\partial y} (\rho_m huv) = -\rho_m gh \frac{\partial B}{\partial x} + F_x - u \left[\sum_{i_s=1}^{n_s} (\rho_{s,i_s} D_{s,i_s}) + \rho_w \left(D_w + \frac{\alpha_d}{1 - \alpha_d} \sum_{i_s=1}^{n_s} D_{s,i_s} \right) \right], \quad (3a)$$

97

$$\frac{\partial(\rho_m hv)}{\partial t} + \frac{\partial}{\partial x} (\rho_m huv) + \frac{\partial}{\partial y} \left(\rho_m hv^2 + \frac{1}{2} \rho_m gh^2 \right) = -\rho_m gh \frac{\partial B}{\partial y} + F_y - v \left[\sum_{i_s=1}^{n_s} (\rho_{s,i_s} D_{s,i_s}) + \rho_w \left(D_w + \frac{\alpha_d}{1 - \alpha_d} \sum_{i_s=1}^{n_s} D_{s,i_s} \right) \right], \quad (3b)$$

98 where $F = (F_x, F_y)$ is the vector of frictional forces and the last term on the right-hand side of both the equations considers
 99 the loss of momentum associated with particle sedimentation. Please note that there are no terms associated with erosion
 100 of solid particles in the momentum equations, because they do not carry any horizontal momentum within the flow,
 101 although they change the inertia terms.

102 Flow temperature T changes with entrainment of water and solid particles eroded from the underlying terrain, and this in
 103 turn can change lahars property (for example viscosity). For this reason, we also solve for a transport equation for the
 104 internal energy $e = C_p T$ (with C_p being the mass averaged specific heat in the flow):

$$\frac{\partial}{\partial t} (\rho_m he) + \frac{\partial}{\partial x} (\rho_m hue) + \frac{\partial}{\partial y} (\rho_m hve) = \sum_{i_s=1}^{n_s} [\rho_{s,i_s} C_{s,i_s} (T_s E_{s,i_s} - T D_{s,i_s})] + \rho_w C_w \frac{\alpha_d}{1 - \alpha_d} \sum_{i_s=1}^{n_s} [(T_s E_{s,i_s} - T D_{s,i_s})] \quad (4)$$

105 where C_s , C_w are the specific heats of solid and water, respectively, and T_s is the substrate temperature before erosion. In
 106 this equation, heat transfer by thermal conduction is neglected, as well as thermal radiation and heating due to friction.

107 Additional transport equations for the mass of n_s solid classes are also considered:

$$\frac{\partial (s_{i_s} \rho_{s,i_s} h)}{\partial t} + \frac{\partial (\alpha_{s,i_s} \rho_{s,i_s} hu)}{\partial x} + \frac{\partial (\alpha_{s,i_s} \rho_{s,i_s} hv)}{\partial y} = \rho_{s,i_s} (E_{s,i_s} - D_{s,i_s}), \quad i_s = 1, \dots, n_s \quad (5)$$

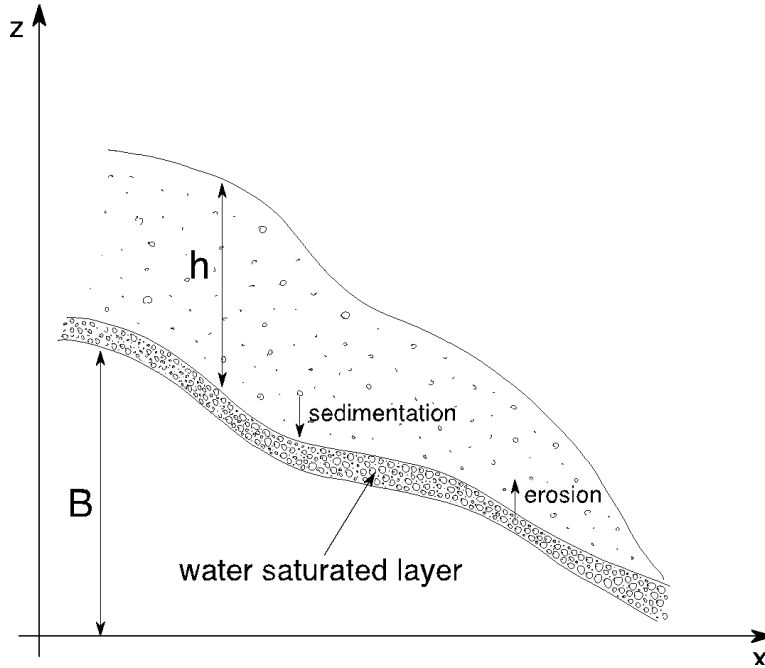
108 Finally, we have n_s equations for the volume of solid particles in the water-saturated erodible layer:

$$\frac{\partial \alpha_{s,i_s} h_{s,i_s}}{\partial t} = (E_{s,i_s} - D_{s,i_s}), \quad i_s = 1, \dots, n_s \quad (6)$$

109 where h_{s,i_s} is the thickness of each solid class in the layer, related to the total thickness h_e of this layer by the
 110 relationship:



$$h_e = \frac{1}{1 - \alpha_w} \sum_{i_s=1}^{n_s} h_{s,i_s} \quad (7)$$



111

112 *Figure 1. Sketch of the lahar.*

113

114 2.1.2. Constitutive equations

115 The set of equations (1-7) constitute a set of $4 + n_s$ partial differential equations for the unknown state variables $Q = h,$
 116 $u, v, T, \alpha_{s,1}, \dots, \alpha_{s,n_s}.$ In order to close the system and to be able to solve the equations, the terms accounting for friction,
 117 deposition, erosion should be defined as functions of the state variables $Q.$

118 The friction term appearing in the momentum equations is written in the following way:

$$F = (F_x, F_y) = \rho_m g h \left(\frac{u}{\sqrt{u^2 + v^2}} s_f, \frac{v}{\sqrt{u^2 + v^2}} s_f \right) \quad (8)$$

119

120 where s_f is defined, accordingly to O'Brien et al. (1993), as the total friction slope, given by the sum of three non-
 121 dimensional terms:

$$s_f = s_y + s_v + s_t. \quad (9)$$



122 Here, s_y is the velocity-independent yield slope, s_v is the viscous slope and s_t is the turbulent slope. These three terms,
 123 as done in the numerical code FLO-2D, are written in the following way:

$$s_f = \frac{\tau_y}{\rho_m g h} + \frac{K \mu \sqrt{u^2 + v^2}}{8 \rho_m g h^2} + \frac{n_{td}^2 (u^2 + v^2)}{h^{4/3}} \quad (10)$$

124 where τ_y is yield strength, K is an empirical resistance parameter, μ is fluid viscosity and n_t is the Manning roughness
 125 coefficient. In FLO-2D model (O'Brien et al., 1993), yield strength τ_y and fluid viscosity μ_m are defined through two
 126 empirical relationships derived from field observations:

$$\mu_m = a_1 \exp(b_1 \alpha_s) \quad (11a)$$

127

$$\tau_y = a_2 \exp(b_2 \alpha_s) \quad (11b)$$

128

129 where a_i and b_i are coefficients defined by laboratory experiments and α_s is the total volumetric fraction of solid ($\alpha_s =$
 130 $\sum_{i_s=1}^{n_s} \alpha_{s,i_s}$). In the original formulation of O'Brien et al., (1993) the empirical parameters a_1 e b_1 are model constants,
 131 which do not vary with flow temperature. Here, we notice that the parameter a_1 has the units of a dynamic viscosity and
 132 it can be seen as the limit viscosity of the mixture when the dispersed solid fraction goes to zero. Thus, it should represent
 133 the dynamic viscosity of water. Commonly this parameter can be assumed to be constant, but in order to account for the
 134 dependence of water viscosity on its temperature, which could potentially affect lahar dynamics and runout, here we
 135 account for an additional correction factor $\Gamma(T^c)$, function of the temperature expressed in Celsius degrees:

$$a_1 = [\mu^{ref} \cdot \Gamma(T^c)]. \quad (12)$$

136

137 where μ^{ref} denotes the viscosity at a reference temperature T^{ref} . Following Crittenden et al. (2012), the equation used
 138 to compute the factor $\Gamma(T^c)$ is given by:

$$\Gamma(T) = C \cdot \gamma \cdot 10^A$$

139

140 where:

$$\begin{cases} \gamma = 10^{-3}, & \text{for } 0 < T^c < 20^\circ C \\ \gamma = (1.002 \cdot 10^{-3})(10^B), & \text{for } T^c \geq 20^\circ C \end{cases}$$

141

$$\begin{cases} A = \frac{1301}{998.333 + 8.1855(T^c - 20) + 0.00585(T^c - 20)^2} - 1.30223 & \text{for } 0 < T^c < 20^\circ C \\ A = \frac{1.3272(20 - T^c) - 0.001053(T^c - 20)^2}{T^c + 105} & \text{for } T^c \geq 20^\circ C \end{cases}$$

142



143 and C is a constant such that $\Gamma(T^{c,ref}) = 1$. With this choice, when $T^c = T^{c,ref}$ and $\alpha_s = 0$, $\mu = \mu^{ref}$. With respect to
 144 the original work of O’Brian et al., (1993), also the original relationship for yield strength has been modified. In fact, here
 145 we take:

$$\tau_y = a_2(\exp(b_2\alpha_s) - 1) \tag{13}$$

146

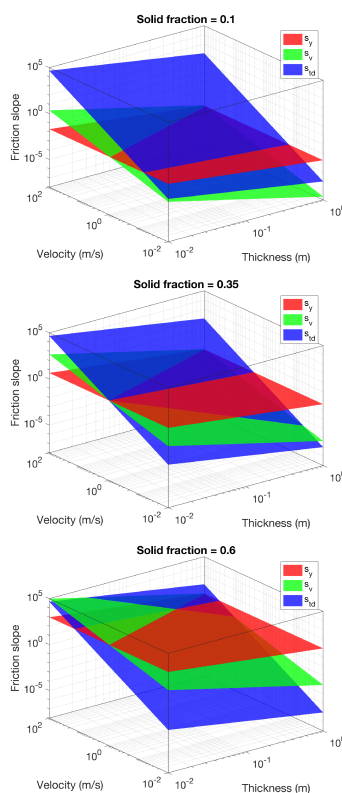
147 In this way, yield stress disappears when solid fraction α_s goes to zero, recovering the Newtonian behaviour of water.

148

149 The values of the three components of the total friction slope (see Eq. 10) strongly depends on volumetric solid fraction,
 150 on flow thickness and velocity. In Figure 2, for fixed values of the empirical parameters a_i and b_i ($i=1,2$) and for three
 151 different values of the total solid volume fraction ($\alpha_s = 0$ on the left; $\alpha_s = 0.25$ in the middle; $\alpha_s = 0.5$ on the right), we
 152 plotted the values of the three terms as function of flow thickness and velocity. These diagrams (in logarithmic scale for
 153 all the variables) highlight how these terms can vary in a non-linear way by several orders of magnitude when thickness,
 154 velocity and solid fraction vary in ranges that can be observed in lahars, potentially resulting in the presence of a stiff
 155 term in the system of equations. For this reason, it is needed a robust solver that allows the coupling between the
 156 gravitational and frictional terms to be accurately simulated.

157

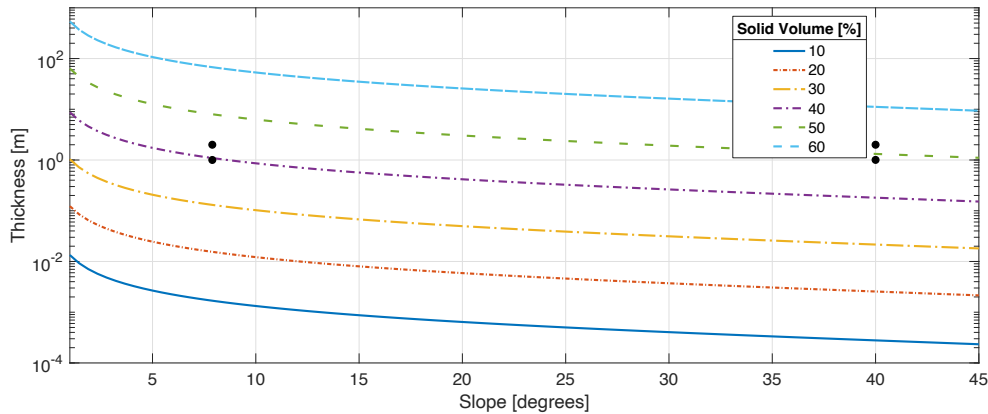
158





159 *Figure 2. Contribution of the yield slope (s_y), viscous slope (s_v) and turbulent slope (s_{td}) to the total friction slope for*
 160 *three different solid volume fractions: 0% (left); 25% (middle); 50% (right). The friction parameters have the following*
 161 *values: $K = 24.0$; $a_1 = 8.9 \cdot 10^{-4}$; $b_1 = 22.1$; $n_t = 0.1$; $a_2 = 0.272$; $b_2 = 22.0$.*

162 We also note that the presence of the yield strength term, i.e. a term independent of the velocity that opposes the motion,
 163 allows the flow to stop with a thickness that depends on the slope of the topography and on the fraction of solid material
 164 in the flow. This critical thickness can be calculated analytically and allows for the validation of the correct
 165 implementation of the discretization of the friction terms in the numerical model. Below we present a figure illustrating
 166 this relationship, where each line represents the critical thickness threshold line between the steady and unsteady condition
 167 for different total solid percentage in the flow. We can see that, approximatively, an increase of 10% in the solid volume
 168 fraction, for a fixed slope, corresponds to a factor 4.5 increase in the critical thickness. We also observe that such a critical
 169 thickness is not only relevant for flow stoppage, but also for the initial triggering of the flow, and that this relationship
 170 can be formulated also in terms of critical liquid volume fraction. Thus, given a thickness of the permeable layer and a
 171 slope, we can compute the critical liquid volume fraction over which the lahar is triggered because the gravitational force
 172 exceeds the yield strength. For example, a slope of 20° and a thickness of 1 m, a 60% liquid volume would trigger a lahar,
 173 while a 50% liquid volume would not. It is also worth to note that these critical thresholds depend on the values of the
 174 parameters for the yield strength.



175 *Figure 3. Critical thickness as a function of topography slope and solid volume fraction computed with the following*
 176 *values for the yield strength parameters: $\alpha_2 = 0.272$; $b_2 = 22.0$. The four black dots represent couples of slope and*
 177 *thickness values used to test the capability of the numerical solver to properly reproduce the triggering conditions of*
 178 *lahars.*

180 2.1.3 Erosion term

181 Following the parameterization by Fagents and Baloga (2006), we adopted an empirical relationship for the volumetric
 182 erosion rate E_{tot} of the substrate:

$$E_{tot} = \epsilon h \sqrt{u^2 + v^2} (1 - \alpha_s). \quad (14)$$



183 This relation states that erosion is proportional to the thickness of the flow, the modulus of flow velocity and the
184 volumetric fraction of water in the flow, through an empirical constant ϵ (with units $1/[L]$). In the original work by Fagents
185 and Baloga (2006), it is assumed that the rate of turbulent entrainment diminishes with increasing flow density. In fact,
186 as the flow entrains solid sediment, turbulence is progressively dampened (Costa, 1988). Here, because the density is
187 linearly proportional to the water volume fraction, we directly introduced a dependence of the erosion rate on this variable.
188 From the total erosion rate, we compute the entrainment rates of the solid phases, which are then used in the governing
189 equations, as:

$$E_{i_s} = \beta_{i_s}(1 - \alpha_d)E_{tot} \quad (15)$$

190 where β_{i_s} are the relative volumetric fractions of the solid particles in the erodible substrate ($\sum \beta_{i_s} = 1$). When erosion
191 occurs, not only solid particles are entrained in the flow, but also the water present in the deposit, here assumed to saturate
192 its voids. This water entrainment from the erodible substrate is given by:

$$E_w = \alpha_d E_{tot}. \quad (16)$$

193

194 2.1.4 Sedimentation term

195 Sedimentation of particles from the flow is modelled as a volumetric flux at the flow bottom and it is assumed to occur
196 at a rate which is proportional to the volumetric fraction of particles in the flow and to the particle settling velocity w_s :

$$D_{s,i_s} = \alpha_{s,i_s} \cdot w_{s,i_s} (d_{s,i_s}, \rho_{s,i_s}, \nu_m). \quad (17)$$

197 The particle settling velocity w_{s,i_s} is a function of the particle diameter d_{s,i_s} , the particle density ρ_{s,i_s} and the mixture
198 kinematic viscosity $\nu_m = \frac{\mu_m}{\rho_m}$, and it is obtained by solving the following non-linear equation:

$$w_s^2(d_{s,i_s})C_D(Re) = \frac{4}{3}d_{s,i_s}g \left(\frac{\rho_{s,i_s} - \rho_a}{\rho_a} \right).$$

199 The gas-particle drag coefficient C_D is a function of the particle Reynolds number ($Re = \frac{d_{s,i_s}w_s}{\nu_m}$), and it is calculated by
200 assuming spherical particles (although in the future can be generalized for more realistic shapes; Bagheri and Bonadonna,
201 2015; Dioguardi et al., 2016) through the following relations (Gidaspow, 1994):

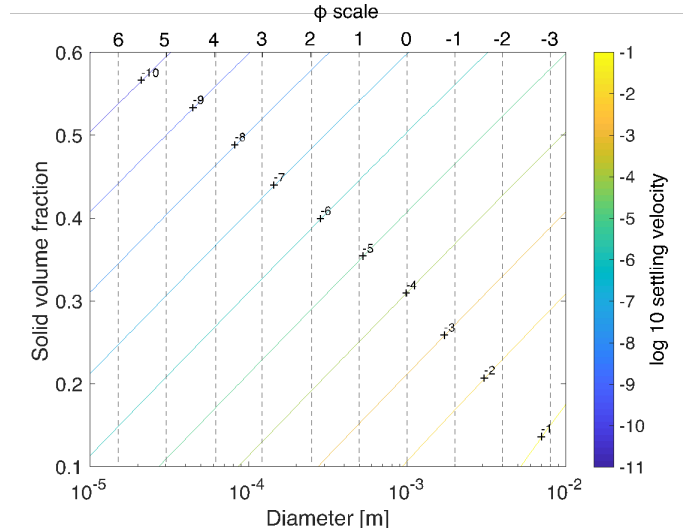
$$\begin{cases} C_D = \frac{24}{Re}(1 + 0.15Re^{0.687}) & Re \leq 1000, \\ C_D = 0.44 & Re > 1000. \end{cases}$$

202

203 The dependence of the Reynolds number on the mixture kinematic viscosity acts on the settling velocity as a sort of
204 hindered settling. In fact, mixture viscosity increases with the total volumetric fraction of solids, and thus the settling
205 velocity decreases. This approach is described in Koo (2009), where several effective-medium models are analysed for
206 determining settling velocities of particles in a viscous fluid. Effective-medium theories have been developed for



207 predicting the transport properties of suspensions consisting of multiple particles in a fluid. In particular, the sedimentation
 208 velocity is computed using the effective viscosity of the suspension, instead of the viscosity of the continuous phase.



209
 210 *Figure 4. Effective settling velocity. Values of the settling velocity are represented by the different contours, as a function*
 211 *of particle diameter and total solid volume fraction.*

212 When considering the settling of solid particles, it is important to remind that we assume the flow deposit formed because
 213 of sedimentation being saturated in water, with the volume fraction of water given by α_w . Thus, the lahar does not loose
 214 solid particles only because of sedimentation, but water too, with the volumetric deposition rate of water related to that
 215 of solid particles by the following equation:

$$D_w = \frac{\alpha_d}{1 - \alpha_d} \sum_{i_s=1}^{n_s} D_{s,i_s} \quad (18)$$

216
 217 **2.2 Numerical implementation**

218
 219 The numerical solution of the equations is based on the algorithm developed by de' Michieli Vitturi et al. (2019) for the
 220 code IMEX-SfloW2D, and in particular on an operator splitting technique, where the advective, gravitational, and friction
 221 terms governing the fluid-dynamics of the lahar are integrated in one step, while the erosion and deposition terms are
 222 integrated in a second step. This allows ad-hoc numerical methods to be used for the different physical processes,
 223 optimizing and simplifying the overall solution process.

224 The numerical integration of the advective, gravitational and frictions terms is based an Implicit-Explicit (IMEX) Runge-
 225 Kutta scheme, where the conservative fluxes and the gravitational terms are treated explicitly, while the stiff terms of the
 226 equations, represented by friction, are integrated implicitly. For the explicit spatial discretization of the fluxes, a modified
 227 version of the finite-volume central-upwind Kurganov and Petrova (2007) scheme has been adopted. The scheme,
 228 described in de' Michieli Vitturi et al. (2019) and Biagioli et al. (2022), has a second-order accuracy in space and
 229 guarantees the positivity of the flow thickness. The spatial accuracy is obtained with a discontinuous piecewise bi-linear
 230 reconstruction of the flow variables, in order to compute their values at the sides of each cell interface and thus the



231 numerical fluxes. The slopes of the linear reconstructions of flow variables in the x - and y -direction are constrained by
232 appropriate geometric limiters, allowing switching between low and high-resolution schemes.
233 The implicit part of the IMEX Runge-Kutta scheme is solved using a Newton-Raphson method with an optimum step
234 size control, where the Jacobian of the implicit terms is computed with a complex-step derivative approximation. The use
235 of an implicit discretization of the stiff friction terms allows for larger time steps, controlled by the CFL condition,
236 establishing a relationship between time step, flow velocity and cell sizes.
237 After each Runge-Kutta procedure, the erosion, deposition, and air entrainment term are integrated explicitly and the flow
238 variables and the topography at the centres of the computational cells are updated.
239 The numerical scheme is also designed to be well-balanced, i.e. to correctly preserve steady-states. This property is
240 important for the numerical simulation of lahars, for which the flow should be triggered only when the gravitational force
241 exceeds the frictional forces, and thus a proper balance of these terms must exist also in the discretized equations resulting
242 from the numerical schemes.

243

244 **3 Model validation and applications**

245

246 In this section we present a few applications of the proposed lahar model aimed at showing its robustness, applicability,
247 and performance. Concerning the numerical tests aimed at demonstrating the mathematical accuracy for the code
248 verification, the reader is addressed to de' Michieli Vitturi et al. (2019) where the code IMEX-SfloW2D, on which our
249 model is based, was presented. Applications of the code to hazard assessment for lahars in the Neapolitan area will be
250 presented in the companion paper by Sandri et al. (2023).

251 Firstly, we present the case of a lahar flow on a synthetic topography in order to investigate the triggering conditions.
252 Secondly, we introduce and describe all the needed variables to perform an application on real topography, that is the
253 Valle di Avella, one of the Apennine valleys adjacent to Mt. Vesuvius, where in the companion papers by Di Vito et al.
254 (this issue) and Sandri et al. (this issue) we also performed geological investigations and hazard analysis for lahar. In such
255 test area we explore the effects that can potentially affect the results, such as computational grid size, numerical scheme
256 order, water temperature, discretization of the grain size distribution, and erosion and deposition terms. As the two latter
257 processes are by far the most relevant on the key output variables such as run-distance, flow thickness and speed, in the
258 last subsection we use field observations to calibrate erosion and deposition terms.

259

260 **3.1 Simulations on a synthetic topography: lahar trigger conditions**

261

262 The first set of simulations we present is aimed at testing the capability of the numerical code to properly reproduce the
263 triggering conditions of a lahar, in terms of the relationship between initial thickness, solid fraction and slope. As
264 previously stated, the values of the friction parameters controlling the yield strength define a unique relationship between
265 thickness, slope and solid fraction resulting in a threshold for the mobility of the flow (see Fig. 2).

266 For the tests we consider a high- and low-angle slope (5 and 40 degrees respectively) and two values of the initial thickness
267 (1 and 2 meters) with different values of the solid fraction (30% and 40%).

268 The topography has a constant slope for $x < 0$ m and is flat for $x > 0$ m. In the left region of the domain, from $x = -55$ m to
269 $x = -50$ m, the topography is excavated with a constant depth (1 or 2 meters). Then, from $x = -50$ m, this region is connected
270 to the original topography with a quadratic function, in order to have a smooth transition and a horizontal slope at the
271 right end. The excavated volume is then filled with the liquid/solid mixture. In this way the free surface elevation of the



272 initial volume corresponds to the original topography elevation. The topography and the free surface are shown in the
273 panels of Fig. 5 with cyan and orange solid lines, respectively.

274 For this suite of tests, both erosion and sedimentation are neglected, in order to have a constant solid volume fraction
275 during the simulations and thus a better understanding of its effect on flow mobility. For all the simulations done, we
276 present in Fig. 5 the solutions in terms of the free surface of the flow at $t=100$ s, corresponding to a steady state. In panel
277 (a) the final solution obtained for a slope of 7 degrees, an initial thickness of 1 m and a solid volume percentage of 40%
278 is shown. By looking at the diagram presented in Fig. 3, we can see that the black marker for this combination of slope
279 and thickness lies below the critical curve for 40% solid (purple line), thus the gravitational forces are smaller than the
280 yield strength and the initial volume should not move. Indeed, this is what happens in panel (a), even if a careful analysis
281 shows that on the left part of the volume there is a small change in the final free surface with respect to the initial constant
282 slope. This is an effect of the grid discretization, which results in a large slope for a very small area, over which the flow
283 is mobilized.

284 Panel (b) shows the final solution for the same condition as panel (a), except the initial thickness increased to 2 m. For
285 this thickness, and for a slope of 7 degrees, the marker in Fig. 3 is above the critical curve for 40% solid (purple line), and
286 thus the yield strength of the initial volume does not exceed the gravitational force. The liquid/solid mixture in this case
287 is mobilized with a small runoff of a few meters at $t=100$ s. Both the flow thickness and the free surface slope decrease,
288 leading to a new steady condition reached when the flow momentum is dissipated by the friction forces.

289 Flow mobility increases also by decreasing the solid fraction. This is shown in panel (c), representing the final solution
290 for the same condition as panel (a), except for the solid volume percentage, lowered from 40% to 30%. By looking at the
291 diagram presented in Fig. 3, we can see that for this combination of slope and thickness the black marker lies well above
292 the critical curve for 30% solid volume (yellow line). In fact, the mixture moves along the slope and is able to reach the
293 topography break in slope, where most of the initial volume has reached a stable condition at $t=100$ s. We observe that a
294 small portion of the flow is left at the base of the excavated area.

295 In the right panels of Fig. 5, a similar analysis is presented for a slope of 40 degrees. The first two simulations we present
296 are done with 50% solid volume (Fig. 3, green line), and initial thickness slightly below (1 m) and above (2 m) the critical
297 thickness for flow mobility. These initial conditions are represented by the right markers in Fig. 3. Fig. 5 (b) shows that,
298 as expected, with an initial thickness of 1 m the flow does not move and at $t=100$ s the free surface has not changed with
299 respect to the initial condition, represented by the free surface parallel to the unmodified topography. When the initial
300 thickness is increased to 2 m (Fig. 5d), the flow starts to move with a final runoff of a few meters only at $t=100$ s, because
301 of the high yield strength associated with the large solid fraction. An initial thickness of 1 m, associated with a 30% solid
302 volume, results in a flow capable of moving along the 40 degrees slope leaving no deposit behind it, as shown in Fig. 5
303 panel (f). In fact, in this case, almost the whole initial volume reaches the flat part of the topography, with a long runoff
304 and a thin deposit due to the speed gained by the flow on the high-slope region.

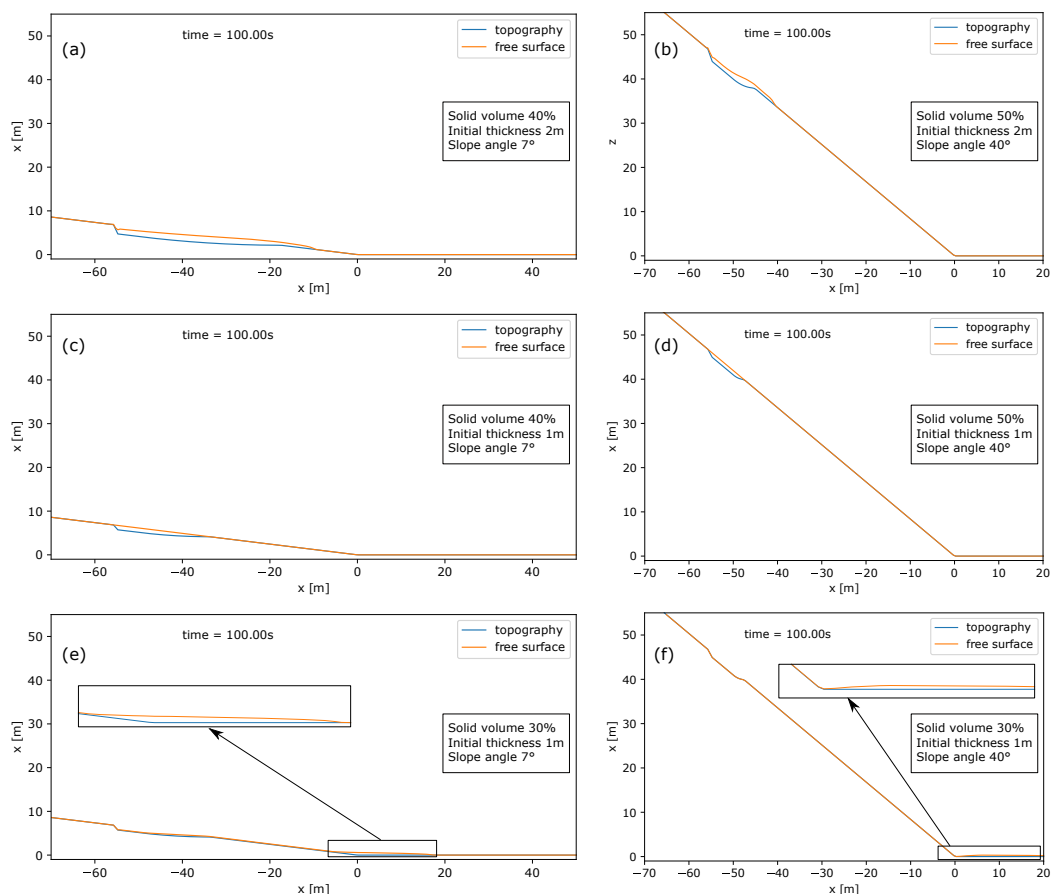
305

306

307



308



309

310 *Figure 5. Flow free surface (red line) and topography (blue line) for 6 simulations with different initial solid volume and*
 311 *thickness and different slope.*

312

313 **3.2 Application to real topography: variables definition**

314

315 As an application of the model, we consider a syn-eruptive lahar from a medium-sized eruption at Somma-Vesuvius, that
 316 is characterized by a total erupted mass between 10^{11} and 10^{12} kg (Macedonio et al., 2016; Sandri et al., 2016). To this
 317 aim, as test case, we selected a synthetic deposit taken from one of the tephra fallout simulations made using the code
 318 Hazmap (Macedonio et al., 2005) presented by Sandri et al. (2016); we considered a lahar generated by heavy rainfall
 319 and we modelled the dynamics of the lahar in the Valle di Avella. In Sandri et al. (2016) a large number of tephra fallout
 320 simulations were performed for a Probabilistic Volcanic Hazard Analysis by varying the wind field and the size and
 321 intensity of the eruption. Among those, we selected a simulation that produced a substantial deposit (of the order of a few
 322 decimetres) on the Apennine flanks facing the Valle di Avella. The Eruption Source Parameters associated to this
 323 simulation are an eruptive-column height equal to 10.9 km, a mass eruption rate equal to 2.89×10^6 kg/s, a duration of the



324 fallout phase of 10 hours and total erupted mass as tephra fallout equal to 1.04×10^{11} kg. The wind conditions are those
325 reported in the ERA5 reanalysis database for 14 December 2001.

326 For a correct modelling of the areas invaded by lahars it is necessary to use a digital terrain model (DEM) as accurate as
327 possible, such as that described in the companion paper by Sandri et al. (2023) which is used for this application.

328 For real life applications, a critical element in the definition of the initial conditions of a syn-eruptive lahar is the proper
329 identification of the areas of the topography where a lahar can be triggered, and the lahar's initial volume.
330 As regards the former, as already seen, the terrain slope is a key factor. On the basis of empirical observations, we assume
331 that lahars cannot be generated if the slope is: (i) less than a minimum threshold angle for remobilization (θ_{min}), or (ii)
332 greater than an upper threshold angle (θ_{max}), which prevents the accumulation, during the deposit phase of fallout
333 material, and which therefore cannot be remobilized by rainfall later to generate a lahar. The slope angle θ_{max} is fixed
334 here at 40 degrees (Bisson et al. 2014). As explained in the companion paper by Sandri et al. (2023), the value of the
335 lower threshold depends on the local granulometry and other factors that are necessary to be considered for a hazard
336 quantification in order to consider the uncertainty associated with this parameter. For this application we fixed $\theta_{min} =$
337 30° . Thus, on our computational grid we consider as possible source of the lahar only the cells with a slope between 30°
338 and 40° .

339 As regards the initial lahar volume, this is a consequence of the initial remobilization thickness h_{tot} (see Figure 6 for a
340 graphical representation of the variables related to thicknesses and porosity) and of the area of remobilization. In turn,
341 h_{tot} mostly depend on two parameters:

- 342 • the thickness of available compacted deposit, h_s (i.e., devoid of the water filling its pore); in this application the
343 fallout deposit thickness is given by the ground tephra load provided by the Hazmap simulation, and selected
344 from Sandri et al. (2016);
- 345 • the amount of available water, denoted by h_r . Analysing the time series of rainfall at the OVO station located at
346 the historical site of the Vesuvian Observatory since 1940 and the data shown by Fiorillo and Wilson (2004), the
347 maximum rainfall was of the order of few tens of cm (the maximum recorded was 50 cm fallen in 48 hours near
348 Salerno on 26-10-1954). For this application we set the thickness of rainwater available to mobilize the water-
349 saturated deposit to $h_r = 0.5$ m, i.e., equal to the maximum recorded value. We stress that this is a conservative
350 choice, since lahars can also originate with less rainwater available, but in such cases their initial thickness (and
351 thus, volume) will be smaller. However, we also acknowledge that we are not accounting for the expected
352 increases in the maximum rainfall in a few hours, due to global warming, that are becoming more and more
353 frequent during the current decade (Esposito et al., 2018, Vallebona et al., 2015).

354

355 Let us call h_w the thickness of the water layer that we could extract from the water-saturated deposit; then h_w and h_s can
356 be respectively expressed as a fraction of the thickness of the water-saturated deposit, h_d , which has a porosity α_d , as:

$$h_w = h_d \alpha_d \quad (19)$$

357

358 and

$$h_s = h_d (1 - \alpha_d) \quad (20)$$

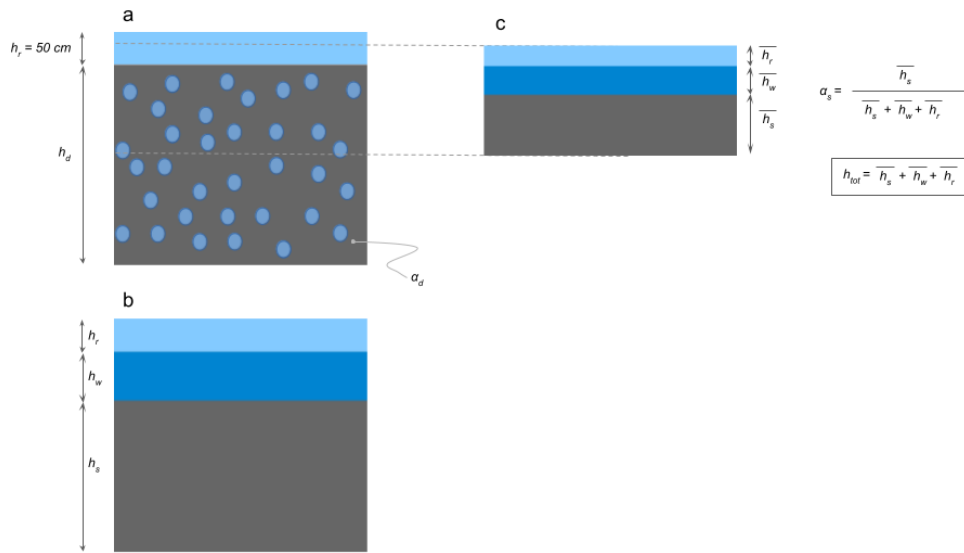
359

360

361



362



363 *Figure 6. Definition of the variables used to define the initial thickness mobilizable h_{tot} . (a) The water-saturated deposit*
 364 *of thickness h_d , with porosity α_d , and the layer of rain water available of maximum thickness $h_r = 50$ cm (assumed). (b)*
 365 *same as in (a) but if we imagine to extract all the pore-filling water and separate it into a layer of water of thickness h_w ,*
 366 *and a layer of compacted deposit of thickness h_s , which is the tephra fallout deposit simulated by Hazmap simulator, in*
 367 *this study. (c) the thickness of the mobilizable layers of deposit \bar{h}_s , rain water \bar{h}_r and pore-filling water \bar{h}_w depends on*
 368 *the availability of rain and deposit and the fixed solid fraction α_s of the initial flow.*

369

370

371 The initial flow thickness that is remobilized, h_{tot} , will be the sum of three thicknesses:

372

373

374

375

376

377

- $\bar{h}_s \leq h_s$ from the solid part of the deposit,
- $\bar{h}_w \leq h_w$, from the water already filling the pores, and
- $\bar{h}_r \leq h_r$, from the rain (as said above, we assume $h_r = 0.5$ m).

There are relations linking these three addends. In particular, due to the condition of water saturation in the deposit

$$\alpha_d = \frac{\bar{h}_w}{\bar{h}_s + \bar{h}_w}, \tag{21}$$

378

379

380

so that

$$\bar{h}_w = \frac{\alpha_d}{(1 - \alpha_d)} \bar{h}_s. \tag{22}$$

381

382

383

384

Moreover, in the initial flow volume there is a relationship between water and solid content, in terms of initial volumetric fraction α_s :



$$\alpha_s = \frac{\bar{h}_s}{\bar{h}_s + \bar{h}_w + \bar{h}_r} \quad (23)$$

385

386 so that (combining equation 22)

387

$$\bar{h}_r = \frac{(1 - \alpha_s)}{\alpha_s} \bar{h}_s - \frac{\alpha_d}{(1 - \alpha_d)} \bar{h}_s = \frac{1 - \alpha_d - \alpha_s}{\alpha_s(1 - \alpha_d)} \bar{h}_s \quad (24)$$

388

389 We see from equations 22 and 24 that both \bar{h}_w and \bar{h}_r are linear functions of \bar{h}_s . Considering the initial availability of
390 remobilizable deposits, we can state that

391

$$\bar{h}_w + \bar{h}_s \leq h_d \quad (25)$$

392

393 or, using equation 22,

394

$$\bar{h}_s \leq (1 - \alpha_d)h_d \quad (26)$$

395

396 Considering, on the other hand, the available water from rain, we have

$$\bar{h}_r \leq h_r \quad (27)$$

397

398 or, using equation 24,

399

$$\bar{h}_s \leq \frac{(1 - \alpha_d)\alpha_s}{(1 - \alpha_d) - \alpha_s} h_r \quad (28)$$

400

401 The maximum solid thickness \bar{h}_s that can be remobilized, considering the availability of water-saturated deposits and
402 rain, and the a priori sampled initial solid fraction α_s , is then the maximum satisfying both conditions in equations 26
403 and 28, i.e.:

404

$$\bar{h}_s \leq \min \left\{ \frac{(1 - \alpha_d)\alpha_s}{(1 - \alpha_d) - \alpha_s} h_r; (1 - \alpha_d)h_d \right\} \quad (29)$$

405

406 Once this is known, we can get the total initial thickness of the lahar, by simply computing it as

$$h_{tot} = \frac{\bar{h}_s}{\alpha_s} \quad (30)$$

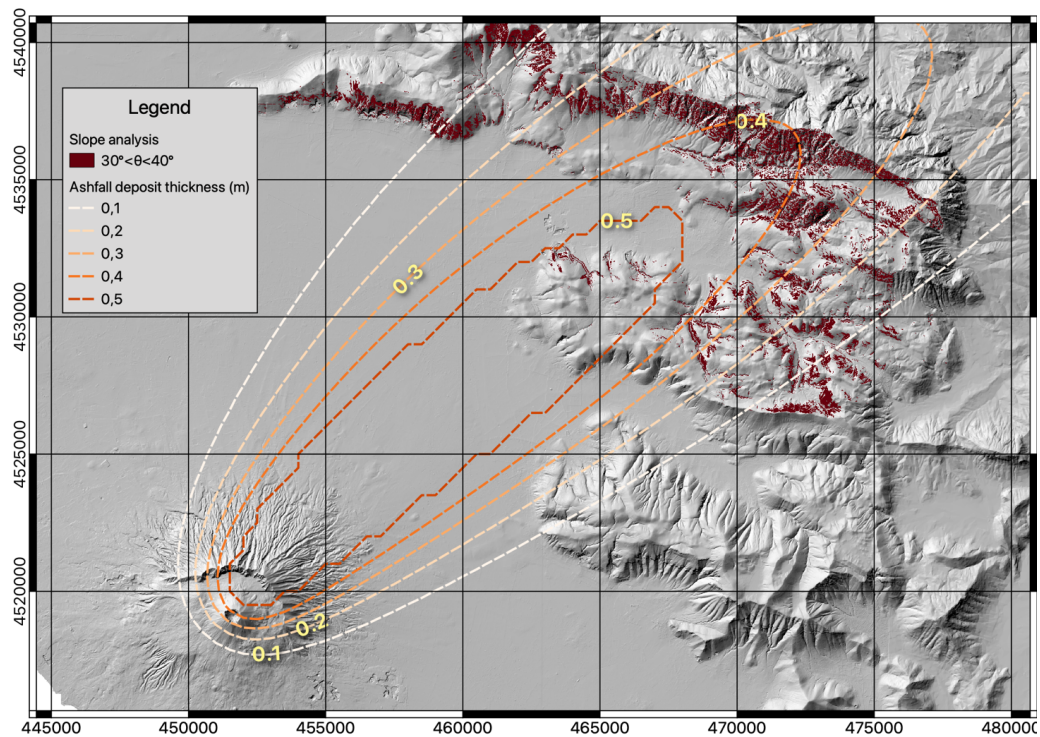
407

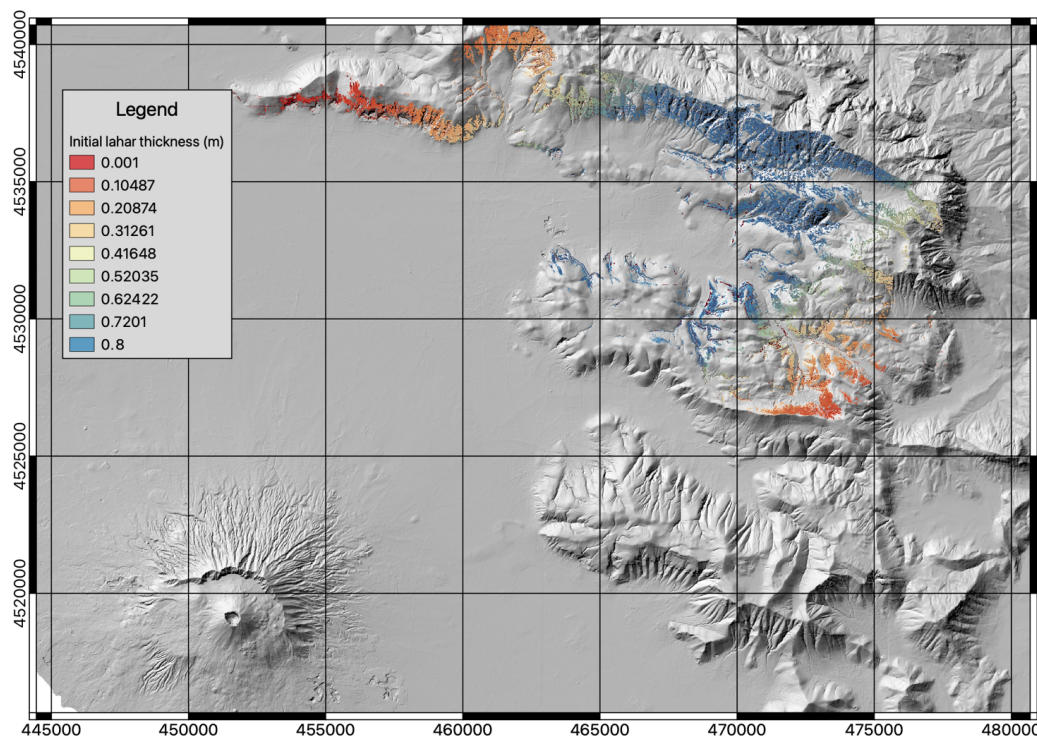
408 The ashfall deposit which does not contribute to the initial volume of the lahar is added to the pre-existing topography as
409 an erodible layer. The contribution of the ash fall deposits in the intermediate and distal areas has been significant in the
410 past sub-plinian eruptions, as shown in the paper by Di Vito et al. (this issue).

411 The steps described above are represented in Figure 7 for the real-topography test application to Valle di Avella, from the
412 identification of areas “prone” to remobilization on the basis of geomorphological features, the terrain slope (top panel,



413 red pixels), to the application of the criterion in equation 29 and 30 to compute the initial thickness of lahar (bottom panel)
414 from the rainwater available and the ashfall deposit (top panel, contour lines). For the case presented in Figure 7 we
415 assumed a deposit porosity $\alpha_d = 0.22$ and an initial solid fraction in the lahar $\alpha_s = 0.29$. With these values, equations
416 29 and 30 give, for an ashfall deposit thickness of 0.4m and an amount of rain of 0.5m, an initial lahar thickness of
417 approximately 0.8m.
418 Concerning the grain size distribution of the remobilized deposits here we used that obtained by Di Vito et al. (this issue)
419 on the basis of field data analysis.





420

421 *Figure 7. Steps for the definition of the initial lahar thickness. The top panel shows grid cells with slope between θ_{min}*
 422 *and θ_{max} (red pixels) and the HAZMAP deposit thickness (contour lines). The bottom panel shows the initial lahar*
 423 *thickness.*

424 **3.3 Application to real topography: sensitivity tests and description of the relevant output variables**

425

426 We conduct a series of sensitivity tests on the real-topography test area, in order to quantify the relevance of different
 427 terms and processes on the output of the simulations, in terms of flow thickness and/or area.

428 We first present a reference simulation, extracted from the ensemble of simulations presented in Sandri et al. (this issue),
 429 and for this case we show the temporal evolution of the flow and the most relevant output produced by the model. Then,
 430 with respect to this simulation, we vary several parameters to show the sensitivity of the results to several model
 431 parameters.

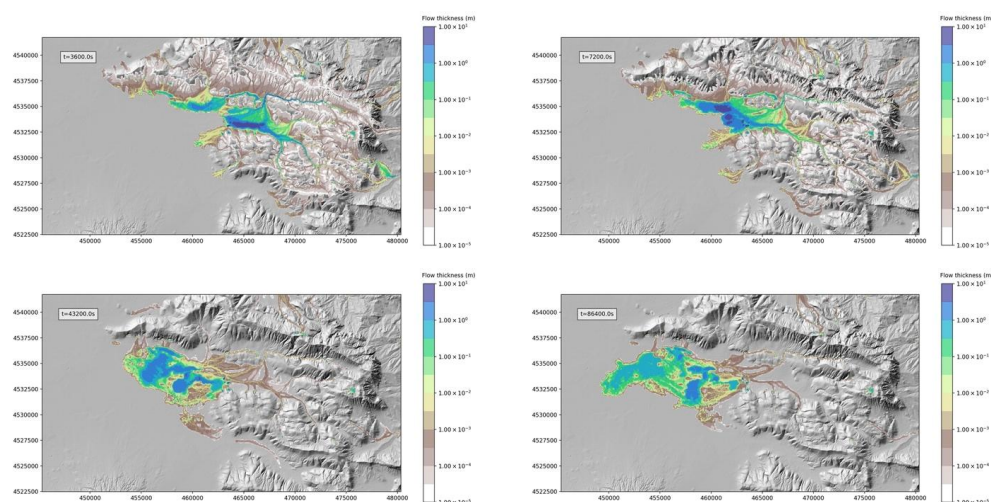
432

433 **3.3.1 Flow evolution and relevant output**

434 In this section we describe a reference simulation, obtained for a computational grid with cells of 50m and a second-order
 435 numerical scheme in space, by applying a van Leer slope limiter to the reconstruction of the flow variable. For this
 436 simulation, the total grain size distribution is discretized with 6 bins, from $\phi = -3$ to $\phi = -7$, and we assume an initial
 437 temperature of the lahar of 373K. While we recognize that this temperature is more adequate for syn-eruptive lahars from
 438 pyroclastic density current deposits, here we used this value to better show the effect of the temperature on the lahar
 439 dynamics. In fact, later in the paper, we compare the results with those obtained with a colder lahar (300K).



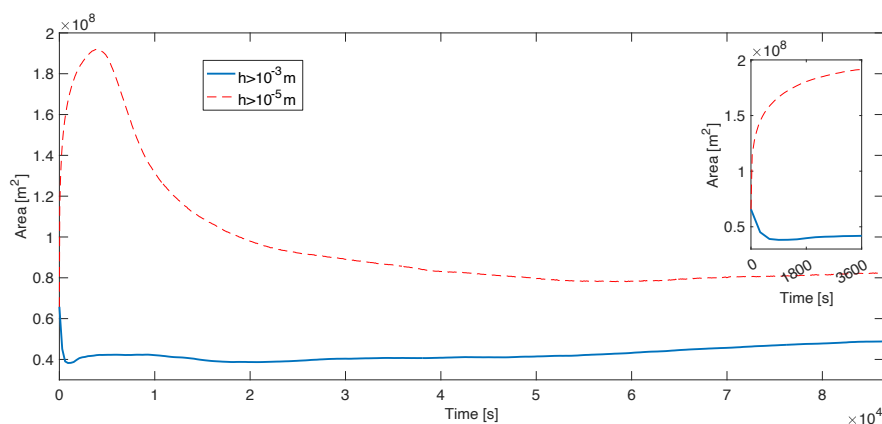
440



441 *Figure 8. Lahar thickness temporal evolution: top-left at 3600s; top-right at 7200s; bottom-left at 43200s; bottom-right*
 442 *at 86400s.*

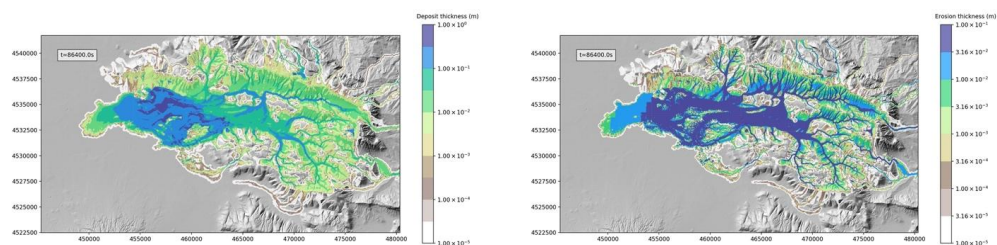
443 The initial thickness of the lahar is shown in the bottom panel of Figure 7, and its temporal evolution is presented in the
 444 four panels of Figure 8. After one hour from the mobilization (Figure 7, top-left panel) the lahar already invaded a large
 445 portion of the Valle di Avella, with its maximum thickness reaching a few meters in its southern part, and a thickness of
 446 few millimetres still moving on the flanks of the Apennines facing the valley.

447 After 1 hour of flow time, the lahar has already reached the localities of Avella, Roccarainola and Camposano, which all
 448 are inside the case-study valley, while after 2 hours the lahar has reached the city of Nola, just outside the valley. After
 449 12 hours of flow time, the lahar has already reached the localities of Marigliano and Cancellò Scalo, the first being in the
 450 more open plain, while the second nearby the NWW Apennine sector of the valley. After 24 hours of flow time, the lahar
 451 has already reached the city of Acerra in the open plain. Although this simulation is not aimed at reproducing a particular
 452 event from the past, but at showing the model's ability to describe the different phenomena that may characterize a future
 453 lahar in the Avella Valley, it is interesting to note that these reaches are corroborated by some historical sources on the
 454 "1631" events, for which it is reported that the localities of Marigliano and Nola were reached by those lahars and by
 455 geological evidences reported in Di Vito et al. (this issue).



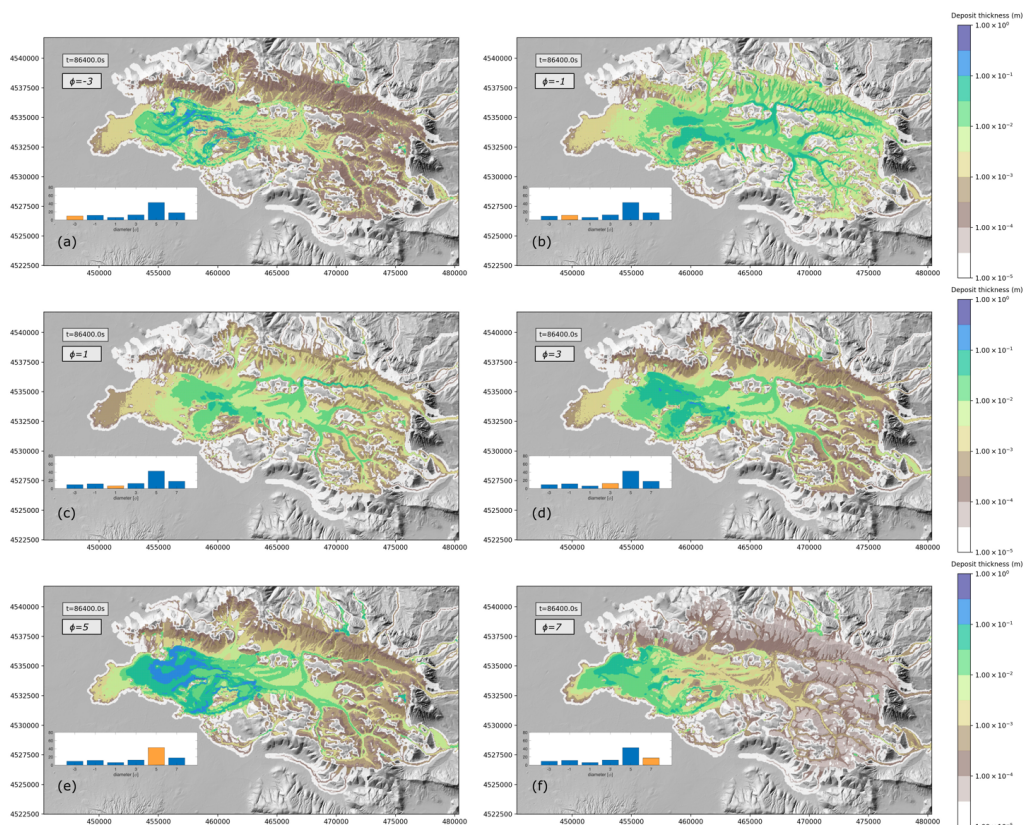
456
 457 *Figure 9. Area of the lahar versus time for the reference simulation. For the computation of the area two thresholds on*
 458 *thickness have been applied: a physical one (solid blue line, $h \geq 10^{-3}$ m), and a numerical one (dashed red line, $h \geq$*
 459 *10^{-5} m). The inset represents a detail of the first hour of simulation.*

460 The area invaded by the lahar changes with time and its evolution is presented in Figure 9. The model computes at each
 461 time step the invaded area as the sum of the areas of the grid cells where flow thickness is greater than a fixed threshold.
 462 For this analysis, two thresholds on the minimum flow thickness have been applied, a “physical” threshold set to 10^{-3} m
 463 (represented in Figure 8 by the solid blue line), which allows to analyse the dynamics of the bulk of the lahar, and a
 464 “numerical” threshold set to 10^{-5} m (represented by the dashed red line). It is important to remark that such a small
 465 threshold does not correspond to a thickness for which the flow is properly described by our model equations, because
 466 for such values forces like surface tension becomes larger than gravity and friction (Hong et al., 2016). In any case, this
 467 small threshold can provide information on the dynamics of the very thin tail of the lahar, where the velocity goes rapidly
 468 to zero because of friction forces. Figure 9 shows that, for the larger physical threshold, at the beginning of the simulation
 469 (first 15 minutes) there is a rapid decrease in the area, due to the channelization phase of the flow mobilized from the flanks
 470 of the Apennines. After this initial phase, the flow reaches the Valle di Avella and starts to spread out, with the area of
 471 the lahar increasing with time. For the lower thickness threshold, we observe that the area rapidly increases during the
 472 initial slumping phase of the lahar and it reaches its maximum after approximately 1 hour after the mobilization. Then it
 473 decreases, first rapidly and then more slowly, increasing again after 15 hours. This is due to the fact that tail of the flow
 474 gets thinner with time and, as previously described, the presence of the yield strength term in the friction allows the flow
 475 to stop with a thickness that depends on the slope of the topography and on the fraction of solid material left in the flow.
 476 Thus, when the thickness is small enough, the tail of the lahar slows down and stops moving. Because of that, erosion
 477 becomes negligible and at the same time deposition occurs, further increasing the thinning of the deposit and the loss of
 478 sediments and water by the flow. This is well shown by the evolution of flow thickness on the flanks of the Apennines,
 479 as illustrated in Figure 8. After one hour from the mobilization, thickness is less than 1 millimetre and, for the slope of
 480 the Apennines and the water content of the flow, this value is well below the critical thickness (see Figure 3). Because of
 481 that, the flow stops to move and the only process occurring is the loss of water and sediments.
 482



483 *Figure 10. Total deposition (left) and erosion (right) after 24 hours of simulation.*

484 The mobility of the flow is mostly controlled by the solid fraction within the lahar, and this fraction can change because
 485 of erosion and deposition. Thus, the total erosion and deposition are important factors controlling the area invaded by the
 486 lahar. The final deposit and erosion thickness are presented in the left and right panels of Figure 10, respectively, showing
 487 a significant erosion where the flow is channelized, reaching a maximum value of a few decimetres. Conversely,
 488 deposition mostly occurs in the flat areas invaded by the lahar where the flow slows down, producing a maximum deposit
 489 thickness of the order of 1m.



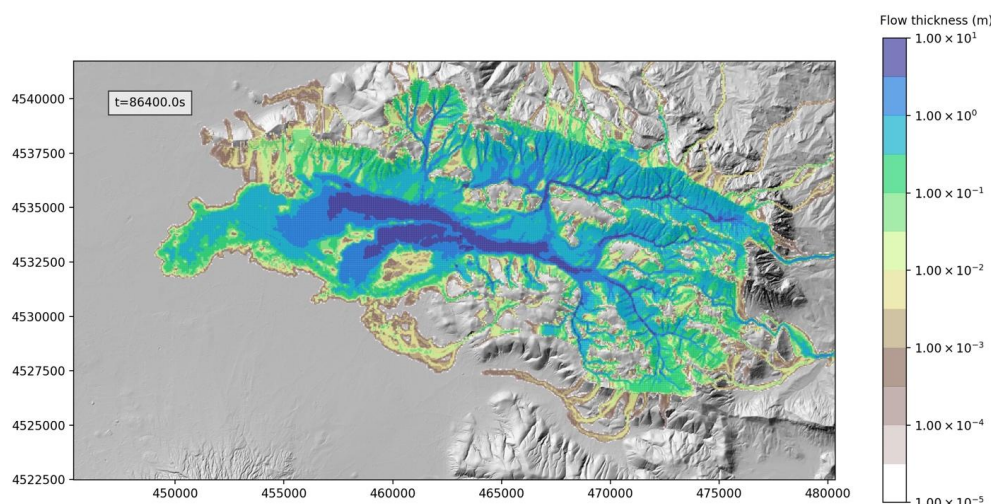
490
 491 *Figure 11. Total deposit thickness after 24 hours of simulation for the 6 different classes of particles: (a) $\phi = -3$; (b)*
 492 *$\phi = -1$; (c) $\phi = 1$; (d) $\phi = 3$; (e) $\phi = 5$; (f) $\phi = 7$. The insets in each panel show the initial total grain size*
 493 *distribution of the lahar, and the class for which the deposit is shown in the panel is represented in orange.*



494

495 As shown by equation 17, deposition is proportional to the settling velocity of the sediments, which increases with their
 496 sizes. This reflects in different depositional patterns for the different classes of particles, shown in the panels of Figure
 497 11. We observe that the thickness of the deposit for the different classes does not depends only on the settling velocities,
 498 but also on the amount of sediments available for deposition, and thus on the initial grain size distribution of the lahar.
 499 This explains why the larger contribution to the deposit is given by class $\phi = 5$, for which the maximum thickness deposit
 500 24 hours after the mobilization of the lahar is about 1 m. For classes $\phi = -3$ and $\phi = -1$ the initial mass fractions are
 501 similar, and the difference in the final deposit is mostly due to the differences in settling velocities. In fact, Figure 4 shows
 502 that, for the same total solid volume fraction of the lahar, a difference in size in the Krumbein scale of 2ϕ results in a
 503 difference in the settling velocity, and thus in the deposition rate, of one order of magnitude.

504



505

506 *Figure 12. Maximum thickness of the flow in each cell of the computational grid during the 24 hours of simulation.*

507 From the perspective of hazard assessment, it is not important the flow thickness at the end of the simulation (here 24
 508 hours after the mobilization), but the maximum thickness registered at each location reached by the lahar in the same time
 509 span, as shown in figure 12. This figure shows that the maximum thickness can exceed several meters over a large area
 510 of the domain, allowing to identify the areas where the hazard is significant.

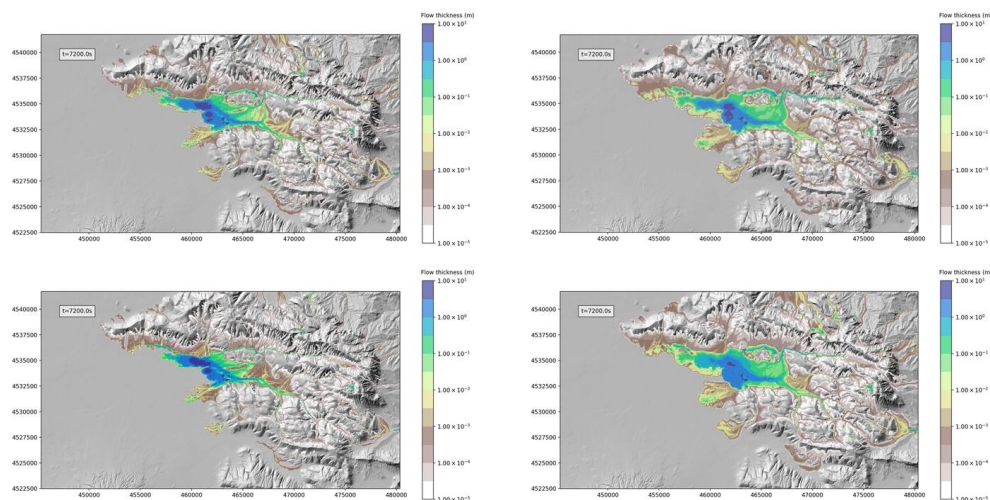
511

512 3.3.2 Effects of grid size and numerical scheme order

513 In this section we want to present the effects of the resolution of the computational grid and of the spatial numerical
 514 scheme adopted (first and second order schemes). We remind that the DEM resolution used for the simulations is 10 m,
 515 while the computational grid resolution used for the reference simulation presented in the previous section was 50m.
 516 Thus, the smaller topographical features present in the original DEM are smoothed in the computational grid, possibly
 517 with an effect on the dynamics of the simulated flow. Here, we focus our interest to the first 2 hours of the simulation,
 518 thus the phase where the details of the topography can be more important, because of the important canalization effects
 519 acting on the lahar when moving down the flanks of the Apennines into the Valle di Avella. All the simulations for this
 520 analysis have been performed on 16 cores of a Multicore shared memory server SuperMicro 4×16-core AMD 2.3 GHz.



521



522 *Figure 13. Maps of flow thickness at $t=7200s$ for simulations with different grids or different numerical schemes: (a)*
 523 *50m grid resolution and 2nd order scheme with geometric limiter; (b) 100m grid resolution and 2nd order scheme with*
 524 *geometric limiter; (c) 25m grid resolution and 2nd order scheme with geometric limiter; (d) 50m grid resolution and*
 525 *1st order scheme (no geometric limits used).*

526

527 In Figure 13 we compare the flow thickness of the reference simulation (top-left) with: a simulation obtained with a 100m
 528 resolution computational grid (top-right); a simulation obtained with a 25m resolution computational grid (bottom-left);
 529 a simulation with a 50m resolution computational grid but with a first-order spatial scheme (bottom-right). While there is
 530 a remarkable difference in the area invaded by the flow between the reference 50m simulation and the 100m simulation,
 531 the difference between the reference simulation and the 25m one, in particular for significant flow thicknesses, is very
 532 small. We also have to account that theoretically the computational time required for a simulation, when the grid cell size
 533 is decreased by a factor 2, increases by a factor 2^3 . In fact, the number of horizontal cells increases by a factor 2^2 , being
 534 the simulation two-dimensional, and the time step decreases by a factor 2, due to the well-known linear relationship
 535 between spatial and temporal step associated with the use of an explicit integration scheme (CFL condition, Courant et
 536 al. 1928). In addition to this, the CPU time required for the initialization of the arrays and for the input/output procedures
 537 must be accounted. For this particular case, the 100m, 50m and 25m resolution simulations required 1023s, 6916s, and
 538 50289s, respectively. This suggests that, with the DEM we used, a 50m resolution is adequate for a proper description of
 539 the flow dynamics, also in view of the utilization of the simulations for hazard studies, where a large number of runs is
 540 required and the computational time is an important constrain.

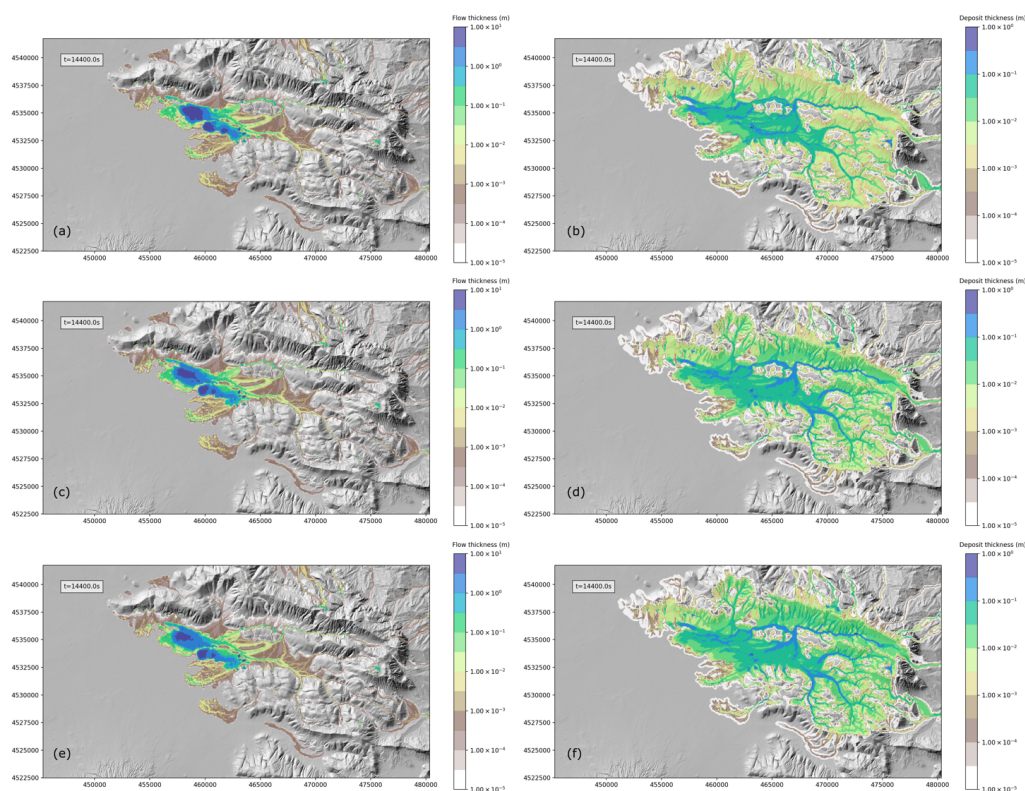
541 Finally, in the bottom-right panel of Figure 13, we can see the output of a simulation with the same resolution of the
 542 reference one (50 m), but without the use of geometrical limiters for the linear reconstruction of flow variables at the
 543 interfaces of the computational cells. This makes the discretization scheme of first order, with respect to the second order
 544 obtained for the reference simulation. The difference in the results is striking, with the first order simulation being more
 545 similar to the simulation obtained with the 100m grid, and the second order simulation being similar to that obtained with
 546 the 25m grid. The computational overhead associated with the use of geometrical limiters is small (6916 seconds vs 6770
 547 seconds), thus their use is strongly suggested for this kind of simulations.



548

549 **3.3.3 Effects of grain size discretization**

550 In this section we present the sensitivity of model results to the discretization of grain size distribution. With respect to
 551 the reference simulation, where 6 classes were used, here we compare the solution after 4 hours from the mobilization of
 552 the lahar with those at the same time for two simulation with the total grain size distribution described by 3 and 12
 553 particle size classes, respectively. The results of this analysis are presented in figure 14, with the final flow thickness presented
 554 on the left panels and the deposit thickness on the right panels. The plots show small differences between the simulations
 555 with 3 (figure 14 a-b) and 6 classes (figure 14 c-d), which become almost negligible when comparing the simulations
 556 with 6 and 12 classes (figure 14 e-f). For this test case, the increase in the number of classes, from 6 to 12, resulted in an
 557 increase of the computational time of a factor 1.3. Thus, the choice of using 6 classes for the reference simulations
 558 represents a good compromise between accuracy and efficiency.



559

560 *Figure 14. Maps of flow thickness (left) and deposit thickness (right) at $t=14400s$ for simulations with different*
 561 *discretization of the total grain size distribution: (a-b) 3 classes; (c-d) 6 classes; (e-f) 12 classes.*

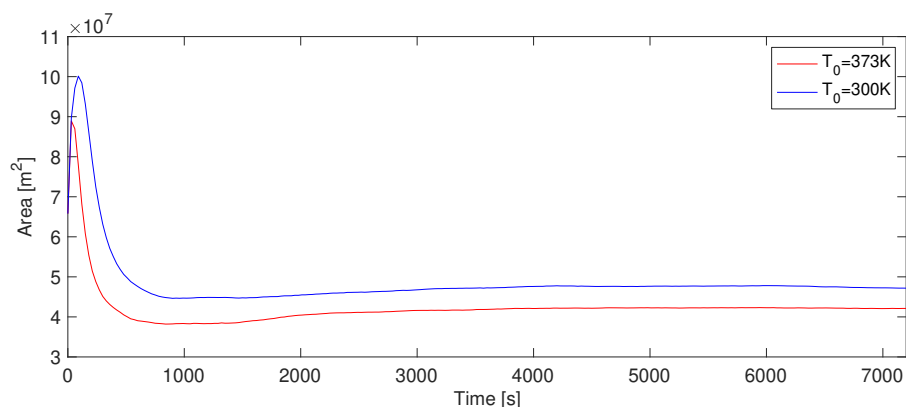
562

563

564 **3.3.4 Effect of initial temperature**

565 In this section we present a comparison between the output of the reference simulation ($T=373K$) and a simulation with
 566 a lower initial temperature ($T=300K$).

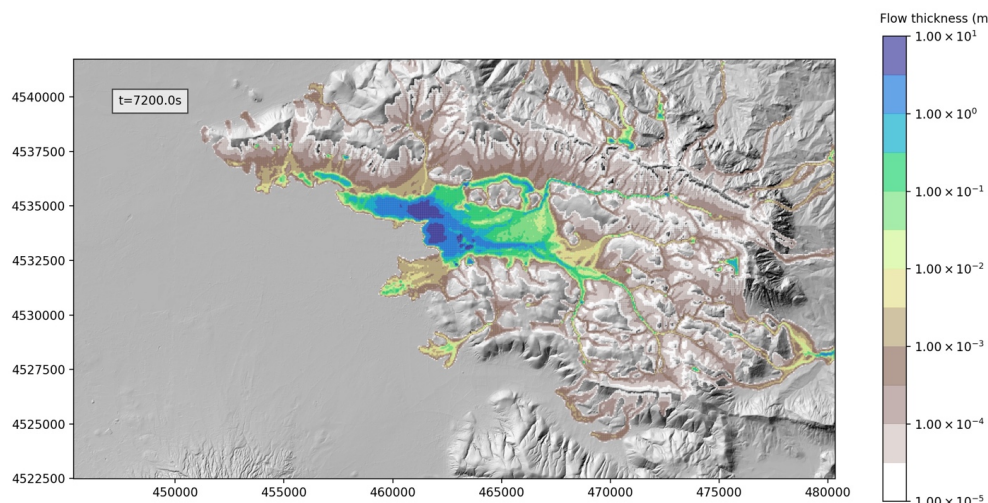
567



568

569 *Figure 15. Area of the lahar versus time for the simulations with different initial temperatures: 300K (blue line) and 373K*
 570 *(red line). The area is computed as the sum of the areas of the grid cells where flow thickness is greater than 10^{-3} m.*

571 Figure 15 shows the invaded area (computed the area as the sum of the areas of the grid cells where flow thickness is
 572 greater than or equal 10^{-3} m) versus time for the two simulations, where the result for the reference simulation is presented
 573 with a red line, while the result for the colder case is plotted with a blue line. We remark that here we are not plotting the
 574 area of the deposit of the lahar, but the area where the lahar is still moving, in order to better understand how flow viscosity
 575 affects the dynamics of the flow. In the initial phase (<60s), the difference between the two cases is negligible, while it
 576 becomes more significant with time, with the area of the colder flow exceeding that of the reference one. This can seem
 577 counterintuitive, because we expect an increased mobility for the hotter flow due to the lower viscosity, and thus a larger
 578 runoff. But the initial phase is dominated by flow channelization, which is increased by the larger mobility, and which
 579 results in a smaller footprint of the lahar. The different viscosity of the flow also affects the tail of the flow in a twofold
 580 way. Indeed, the lower viscosity results in a larger settling the velocity of the sediments and a debulking which further
 581 increases the flow mobility. This is evident by looking at the reduced footprint of the flow left on the Apennines flanks
 582 in the simulation with the higher initial temperature (Figure 12a).



583

584 *Figure 16. Maps of flow thickness at $t=7200$ s for a simulation with an initial temperature $T=300$ K.*



585

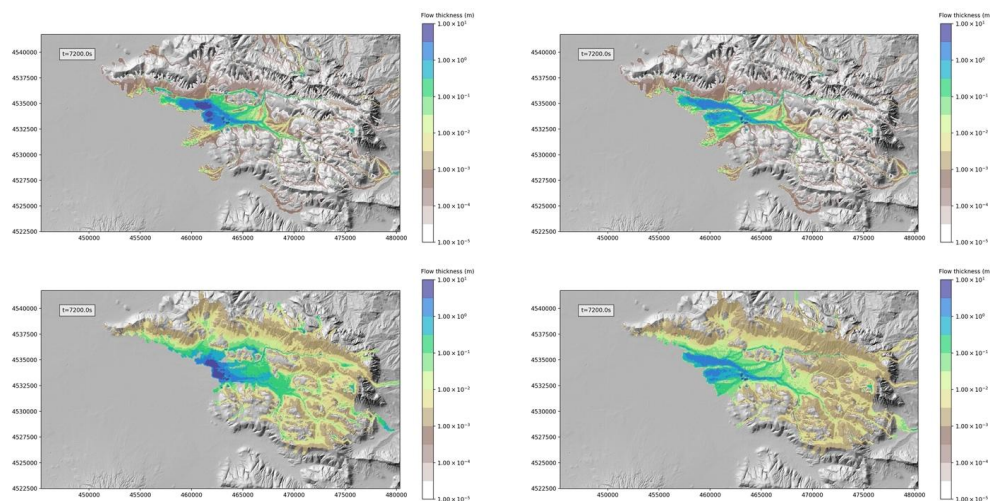
586 3.3.5 Effects of erosion and deposition

587 As shown in the previous comparison, viscosity of the flow has an effect on the debulking process, which in turn can
588 affect the lahar propagation. Here we focus our attention on the effects of the main processes controlling lahar bulking
589 and debulking, i.e. the deposition and erosion processes.

590 This is done by comparing in Figure 17 the first 2 hours of the reference simulation with 3 additional test cases: a
591 simulation without erosion (top-right); a simulation without deposition (bottom-left); a simulation without erosion and
592 deposition (bottom-right).

593 By comparing the flow thickness and the area covered by the flow of the reference simulation and that without erosion,
594 we can see the twofold effect of the bulking associated with erosion. On one hand we observe the larger flow thickness;
595 on the other hand, we observe a smaller runout, due to the lower mobility associated with a higher solid volume fraction.
596 This is particularly true in the Valle di Avella, where the front of the flow advanced about 2km more for the simulation
597 without erosion.

598



599 *Figure 17. Maps of flow thickness at $t=7200s$ for simulations with and without erosion and deposition: (a) reference
600 simulation with erosion and deposition; (b) simulation with deposition and without erosion; (c) simulation with erosion
601 and without deposition; (d) simulation without erosion and deposition.*

602 4 Conclusions

603

604 A new shallow layer model for describing lahar transport was presented. The proposed model does not describe all the
605 general aspects of lahar behaviour (see Pudasaini, 2012) but contains the essential physics needed to reproduce the general
606 features of lahars observed in nature, crucial for assessing their hazard.

607 In particular the model considers realistic particle size distribution, surface erosion and deposition processes through
608 semi-empirical parameterizations calibrated from field data.

609 The model was developed with the aim to describe lahar propagation and deposits and assess their hazard in contexts
610 similar to that of the Vesuvius area, which is highly populated and prone to this kind of phenomenon after heavy rains
611 (e.g., Fiorillo and Wilson, 2004).



612 The critical variables were identified and several sensitivity tests carried out, using synthetic and real cases topographies.
613 The variables used in order to define the source are the initial mobilizable thickness, the water-saturated deposit thickness,
614 the layer of rain water, and the thickness of compacted deposit, which is related to the others through the substrate
615 porosity.
616 The steps used for the assessment of the initial lahar thickness were presented for the real-topography test application to
617 Valle di Avella.
618 The comparison of simulations obtained for different numerical grids (from 25 m to 100 m), scheme order, and grain size
619 discretization were useful to find a good compromise between resolution and computational speed. The used DEM was
620 however at a resolution (10 m) finer than that of the computational grid.
621 The friction term is defined as the sum of a velocity-independent yield slope, a viscous slope, and turbulent slope (O'Brien
622 et al., 1993). The yield strength and the fluid viscosity are considered functions of the total solid volumetric fraction in a
623 consistent way. The values of the three terms strongly depends on volumetric solid fraction, on flow thickness, and
624 velocity. They can vary in a non-linear way by several orders of magnitude when thickness, velocity and solid fraction
625 vary in ranges typical for lahars. This can produce a stiff term in the system of equations, and, for this reason, it is needed
626 a robust solver that allows the coupling between the gravitational and frictional terms to be accurately simulated.
627 Energy transport and temperature effects were also explored in order to better understand how flow viscosity affects the
628 dynamics of the flow. When the friction is dominated by the yield slope term, the difference between the high and low
629 temperature cases is negligible, while it becomes more significant with time, with the area of the colder flow exceeding
630 that of the cold one. In fact, the lower viscosity in the case of the hot flow, beside an increased mobility, results also in a
631 larger settling the velocity of the sediments and a debulking which further increases the flow mobility, producing a
632 reduced footprint deposit area of the flow.
633 Effects of erosion and deposition were investigated by comparing a simulations i) without erosion, ii) without deposition,
634 iii) without erosion and deposition, and iv) with erosion and deposition. By comparing flow thickness and area covered
635 by the flow, we can see the twofold effect of the bulking associated with erosion, that consists in larger flow thicknesses
636 and smaller runouts, due to the lower mobility associated with higher solid volume fractions.
637 The companion paper by Sandri et al. (this issue) will show an application of the presented model for hazard analysis of
638 lahars from Vesuvius deposits in the Neapolitan area.

639

640 **Author Contribution**

641 MdmV, AC and LS defined the set of governing equations of the model. MdmV, LS, AC, MDV and DD defined the
642 equations for the initial conditions. MdmV developed the code. MdmV, LS, AC, MDV and DD defined the set of
643 simulations and MdmV performed them. MdmV prepared the manuscript with contributions from all co-authors.

644

645 **Competing interests**

646 The authors declare that they have no conflict of interest.

647

648 **Acknowledgments**

649 This work has been produced within the 2012–2021 agreement between Istituto Nazionale di Geofisica e Vulcanologia
650 (INGV) and the Italian Presidenza del Consiglio dei Ministri, Dipartimento della Protezione Civile (DPC), Convenzione
651 B2. We also thank Marina Bisson and Roberto Gianardi for providing the DEM used for the simulations.

652



653 **References**

654

655 Aspinall, W.P., Charbonnier, S.J., Connor, C.B., Connor, L., Costa, A., Courtland, L.M., Delgado Granados, H., Godoy,
656 A., Hibino, K., Hill, B.E. and Komorowski, J.C.: Volcanic hazard assessments for nuclear installations: methods and
657 examples in site evaluation, IAEA-TECDOC-1795, IAEA, 2016.

658

659 Bagheri, G.H., Bonadonna, C., Manzella, I. and Vonlanthen, P.: On the characterization of size and shape of irregular
660 particles, Powder Technology, 270, 141-153, <https://doi.org/10.1016/j.powtec.2014.10.015>, 2015.

661

662 Biagioli, E., de' Michieli Vitturi, M., and Di Benedetto, F.: Modified shallow water model for viscous fluids and positivity
663 preserving numerical approximation, Applied Mathematical Modelling, 94, 482-505,
664 <https://doi.org/10.1016/j.apm.2020.12.036>, 2021.

665

666 Costa, J.E.: Rheologic, geomorphic and sedimentologic differentiation of water floods, hyperconcentrated flows and
667 debris flows, in: Flood geomorphology, edited by Baker, V.R., Kochel, R.C. and Patton, P.C., Wiley-Interscience, 113-
668 122, 1988.

669

670 Courant, R., Friedrichs, K. & Lewy, H.: On the Partial Difference Equations of Mathematical Physics, Math. Ann., 100 ,
671 32-74, <https://doi.org/10.1007/BF01448839>, 1928.

672

673 Crittenden, J.C., Trussell, R.R., Hand, D.W., Howe, K.J. and Tchobanoglous, G.: MWH's water treatment: principles and
674 design, John Wiley & Sons, <https://doi.org/10.1002/9781118131473>, 2012.

675

676 Dartevelle, S.: Numerical modeling of geophysical granular flows: 1. A comprehensive approach to granular rheologies
677 and geophysical multiphase flows, Geochemistry, Geophysics, Geosystems, 5(8), Q08003,
678 <https://doi.org/10.1029/2003GC000636>, 2004.

679

680 de' Michieli Vitturi, M., Esposti Ongaro, T., Lari, G. and Aravena, A.: IMEX_SfloW2D 1.0: a depth-averaged numerical
681 flow model for pyroclastic avalanches, Geoscientific Model Development, 12.1, 581-595, <https://doi.org/10.5194/gmd-12-581-2019>, 2019.

682

683 Dioguardi, F. and Mele, D.: A new shape dependent drag correlation formula for non-spherical rough particles.
684 Experiments and results, Powder Technology, 277, 222-230, <https://doi.org/10.1016/j.powtec.2015.02.062>, 2015.

685

686 Di Vito M.A., Rucco I., de Vita S., Doronzo D.M., Bisson M., de' Michieli Vitturi M., Rosi M., Sandri L., Zanchetta G.,
687 Zanella E., Costa A.: Lahar events in the last 2,000 years from Vesuvius eruptions. Part 1: Distribution and impact on
688 densely-inhabited territory estimated from field data analysis, Solid Earth, this issue.

689

690 Esposito, G., Matano, F. and Scepi, G.: Analysis of increasing flash flood frequency in the densely urbanized coastline
691 of the Campi Flegrei volcanic area, Italy, Frontiers in Earth Science, 6, p.63, <https://doi.org/10.3389/feart.2018.00063>,

692

693

2018.



- 694
- 695 Fagents, S. A., and Baloga, S. M.: Toward a model for the bulking and debulking of lahars, *J Geophys Res: Solid*
696 *Earth*, 111.B10, <https://doi.org/10.1029/2005JB003986>, 2006.
- 697
- 698 Fiorillo, F. and Wilson, R.C.: Rainfall induced debris flows in pyroclastic deposits, Campania (southern Italy),
699 *Engineering Geology*, 75(3-4), 263-289, <https://doi.org/10.1016/j.enggeo.2004.06.014>, 2004.
- 700
- 701 Gidaspow, D.: *Multiphase flow and fluidization: continuum and kinetic theory descriptions*, Academic press, 1994.
- 702
- 703 Hong, Y. J., Tai, L. A., Chen, H. J., Chang, P., Yang, C. S., & Yew, T. R.: Stable water layers on solid surfaces. *Physical*
704 *Chemistry Chemical Physics*, 18(8), 5905-5909, <https://doi.org/10.1039/C5CP07866K>, 2016.
- 705
- 706 Iverson, R. M., Schilling, S. P., & Vallance, J. W.: Objective delineation of lahar-inundation hazard zones, *Geological*
707 *Society of America Bulletin*, 110(8), 972-984, [https://doi.org/10.1130/0016-7606\(1998\)110<0972:ODOLIH>2.3.CO;2](https://doi.org/10.1130/0016-7606(1998)110<0972:ODOLIH>2.3.CO;2),
708 1998.
- 709
- 710 Kelfoun, K. and Druitt, T.H.: Numerical modeling of the emplacement of Socompa rock avalanche, Chile, *Journal of*
711 *Geophysical Research: Solid Earth*, 110(B12), <https://doi.org/10.1029/2005JB003758>, 2005.
- 712
- 713 Kelfoun, K., Samaniego, P., Palacios, P. and Barba, D.: Testing the suitability of frictional behaviour for pyroclastic flow
714 simulation by comparison with a well-constrained eruption at Tungurahua volcano (Ecuador), *Bulletin of volcanology*,
715 71(9), 1057-1075, <https://doi.org/10.1007/s00445-009-0286-6>, 2009.
- 716
- 717 Koo, S. and Sangani, A.S.: Effective-medium theories for predicting hydrodynamic transport properties of bidisperse
718 suspensions, *Physics of Fluids*, 14(10), 3522-3533, <https://doi.org/10.1063/1.1503352>, 2002.
- 719
- 720 Kurganov, A., and Petrova, G.: A second-order well-balanced positivity preserving central-upwind scheme for the Saint-
721 Venant system. *Communications in Mathematical Sciences*, 5(1), 133-160,
722 <https://dx.doi.org/10.4310/CMS.2007.v5.n1.a6>, 2007.
- 723
- 724 Lecointre, J., Hodgson, K., Neall, V. and Cronin, S.: Lahar-triggering mechanisms and hazard at Ruapehu volcano, New
725 Zealand: *Natural hazards*, 31(1), 85-109, <https://doi.org/10.1023/B:NHAZ.0000020256.16645.eb>, 2004.
- 726
- 727 Macedonio, G., Costa, A., and Folch A.: Ash fallout scenarios at Vesuvius: Numerical simulations and implications for
728 hazard assessment, *J Volcanol Geotherm Res*, 178, 366–377, <https://doi.org/10.1016/j.jvolgeores.2008.08.014>, 2008.
- 729
- 730 Major, J.J. and Newhall, C.G.: Snow and ice perturbation during historical volcanic eruptions and the formation of lahars
731 and floods, *Bulletin of volcanology*, 52(1), 1-27, <https://doi.org/10.1007/BF00641384>, 1989.
- 732
- 733 Mastin, L.G. and Witter, J.B.: The hazards of eruptions through lakes and seawater, *Journal of Volcanology and*
734 *Geothermal Research*, 97(1-4), 195-214, [https://doi.org/10.1016/S0377-0273\(99\)00174-2](https://doi.org/10.1016/S0377-0273(99)00174-2), 2000.



- 735
- 736 Meruane, C., Tamburrino, A., and Roche, O.: On the role of the ambient fluid on gravitational granular flow dynamics,
737 Journal of Fluid Mechanics, 648, 381–404, <https://doi.org/10.1017/S0022112009993181>, 2010.
- 738
- 739 O'Brien, J. S., Julien, P. Y. and Fullerton, W. T.: Two-dimensional water flood and mudflow simulation, J Hydraulic
740 Engineering 119.2, 244-261, [https://doi.org/10.1061/\(ASCE\)0733-9429\(1993\)119:2\(244\)](https://doi.org/10.1061/(ASCE)0733-9429(1993)119:2(244)), 1993.
- 741
- 742 Patra, A.K., Bauer, A.C., Nichita, C.C., Pitman, E.B., Sheridan, M.F., Bursik, M., Rupp, B., Webber, A., Stinton, A.J.,
743 Namikawa, L.M. and Renschler, C.S.: Parallel adaptive numerical simulation of dry avalanches over natural terrain,
744 Journal of Volcanology and Geothermal Research, 139(1-2), 1-21, <https://doi.org/10.1016/j.jvolgeores.2004.06.014>,
745 2005.
- 746
- 747 Pierson, T.P., Janda, R.J., Thouret, J.C., Borerro, C.A.: Perturbation and melting of snow and ice by the 13 November
748 1985 eruption of Nevado del Ruiz, Colombia, and consequent mobilization, flow and deposition of lahars. J. Volcanol.
749 Geoth. Res. 41, 17-66, [https://doi.org/10.1016/0377-0273\(90\)90082-Q](https://doi.org/10.1016/0377-0273(90)90082-Q), 1990
- 750
- 751 Pitman, E.B., Nichita, C.C., Patra, A., Bauer, A., Sheridan, M. and Bursik, M.: Computing granular avalanches and
752 landslides, Physics of fluids, 15(12), 3638-3646, <https://doi.org/10.1063/1.1614253>, 2003.
- 753
- 754 Pudasaini, S.P.: A general two-phase debris flow model, J. Geophys. Res., 117, F03010,
755 <https://doi.org/10.1029/2011JF002186>, 2012.
- 756
- 757 Pudasaini, S. P., & Mergili, M.: A multi-phase mass flow model, Journal of Geophysical Research: Earth Surface,
758 124(12), 2920-2942, <https://doi.org/10.1029/2019JF005204>, 2019
- 759
- 760 Sandri, L., Costa, A., Selva, J., Tonini, R., Macedonio, G., Folch, A., and Sulpizio, R.: Beyond eruptive scenarios:
761 assessing tephra fallout hazard from Neapolitan volcanoes, Sci Rep, 6, 24271, <https://doi.org/10.1038/srep24271>, 2016.
- 762
- 763 Sandri, L., de' Michieli Vitturi, M., Costa, A., Di Vito, M.A., Rucco, I., Doronzo, D., Bisson, M., Gianardi, R., Sulpizio,
764 R., and Zanchetta, G.: Lahar events in the last 2,000 years from Vesuvius eruptions. Part 3: Hazard assessment over the
765 Campanian Plain, Solid Earth, this issue.
- 766
- 767 Scott, K.M.: Origins, Behavior, and Sedimentology of Lahars and Lahar-runout Flows in the Toutle-Cowlitz River
768 System, U.S. Geological Survey, Professional Paper, 1447-A, <https://doi.org/10.3133/pp1447A>, 1988.
- 769
- 770 Vallance, J.W., and Iverson, R.M.: Lahars and their deposits, in : The encyclopedia of volcanoes, edited by Haraldur
771 Sigurdsson, Academic Press, 649-664, <https://doi.org/10.1016/B978-0-12-385938-9.00037-7>, 2015.
- 772
- 773 Vallebona, C., Pellegrino, E., Frumento, P. and Bonari, E.: Temporal trends in extreme rainfall intensity and erosivity in
774 the Mediterranean region: a case study in southern Tuscany, Italy, Climatic Change, 128(1), pp.139-151,
775 <https://doi.org/10.1007/s10584-014-1287-9>, 2015



776

777 Van Westen, C.J. and Daag, A.S.: Analysing the relation between rainfall characteristics and lahar activity at Mount
778 Pinatubo, Philippines. *Earth Surface Processes and Landforms*, 30(13), 1663-1674, <https://doi.org/10.1002/esp.1225>,
779 2005.

780

781 Zanchetta, G., Sulpizio, R., Pareschi, M.T., Leoni, F.M. and Santacroce, R.: Characteristics of May 5–6, 1998
782 volcaniclastic debris flows in the Sarno area (Campania, southern Italy): relationships to structural damage and hazard
783 zonation, *Journal of volcanology and geothermal research*, 133(1-4), 377-393, [https://doi.org/10.1016/S0377-
784 0273\(03\)00409-8](https://doi.org/10.1016/S0377-0273(03)00409-8), 2004.

785